Features of Structure Formation in an Al–Fe–Mn Alloy upon Crystallization with Various Cooling Rates

I. Loginova, Marjolaine Sazerat, N. Popov, A. Pozdniakov, A. Solonin

▶ **To cite this version:**

I. Loginova, Marjolaine Sazerat, N. Popov, A. Pozdniakov, A. Solonin. Features of Structure Formation in an Al–Fe–Mn Alloy upon Crystallization with Various Cooling Rates. Russian journal of non-ferrous metals, 2021, 62 (1), pp.72-81. 10.3103/S1067821221010119 . hal-03199275

HAL Id: hal-03199275

https://imt-mines-albi.hal.science/hal-03199275

Submitted on 30 Apr 2021

HAL is a multi-disciplinary open access archive for the deposit and dissemination of scientific research documents, whether they are published or not. The documents may come from teaching and research institutions in France or abroad, or from public or private research centers.

L'archive ouverte pluridisciplinaire **HAL**, est destinée au dépôt et à la diffusion de documents scientifiques de niveau recherche, publiés ou non, émanant des établissements d'enseignement et de recherche français ou étrangers, des laboratoires publics ou privés.

Features of Structure Formation in an Al–Fe–Mn Alloy upon Crystallization with Various Cooling Rates

I. S. Loginova[a,b, *, **], M. V. Sazerat[b, c, *], N. A. Popov[a, ****], A. V. Pozdniakov[b, *****], and A. N. Solonin[b, ******]**

[a] *Ural Federal University, Yekaterinburg, 620002 Russia*
[b] *National Research Technological University (MISiS), Moscow, 119991 Russia*
[c] *Institut Mines-Télécom (IMT), Allée des sciences, Mines Albi, 81000 France*
**e-mail: i.s.loginova@urfu.ru*
***e-mail: loginova@misis.ru*
****e-mail: m1911705@edu.misis.ru*
*****e-mail: n.a.popov@urfu.ru*
******e-mail: pozdniakov@misis.ru*
*******e-mail: solonin@misis.ru*

Abstract—Specific features of the microstructure formation of an Al–2.5% Fe–1.5% Mn alloy owing to the cooling rate during casting and during laser melting are studied in this work. An analysis of the microstructure in the molten state shows that, with an increase in the cooling rate during crystallization from 0.5 to 940 K/s, the primary crystallization of the $Al_6(Mn,Fe)$ phase is almost completely suppressed and the volume of the nonequilibrium eutectic increases to 43%. The microstructures of the Al–2.5% Fe–1.5% Mn alloy after laser melting are characterized by the presence of crystals of an aluminum matrix of a dendritic type with an average cell size of 0.56 μm, surrounded by an iron-manganese phase of eutectic origin with an average plate size of 0.28 μm. The primary crystallization of the $Al_6(Mn,Fe)$ phase is completely suppressed. The formation of such a microstructure occurs at cooling rates of 1.1×10^4–2.5×10^4 K/s, which corresponds to the cooling rates implemented in additive technologies. At the boundary between the track and the base metal and between the pulses, regions were revealed consisting of primary crystals of the $Al_6(Mn,Fe)$ phase formed by the epitaxial growth mechanism. The size of the primary crystals and the width of this zone depends on the size of the eutectic plates and the size of the dendritic cell located in the epitaxial layer. After laser melting, the Al–2.5% Fe–1.5% Mn alloy has a high hardness at room temperature (93 HV) and, after heating up to 300°C, it has a high thermal stability (85 HV). The calculated yield strength of the Al–2.5% Fe–1.5% Mn alloy after laser melting is 227 MPa. The combination of its ultrafine microstructure, high processibility during laser melting, hardness at room and elevated temperatures, and high calculated yield strength make the Al–2.5% Fe–1.5% Mn alloy a promising alloy for use in additive technologies.

Keywords: Al–Fe–Mn, additive manufacturing, cooling rate, laser melting, microstructure, hardness

INTRODUCTION

Additive technologies are developing extensively thanks to a number of advantages over conventional methods of fabricating details made out of metallic materials. Their industrial-scale employment allows one to fabricate details possessing complex geometrical shapes, similar to their final configuration, from multicomponent alloys whose composition is chosen with the goal of providing high mechanical and operational characteristics. A large number of works is devoted to the study of new aluminum-based compositions of Al–Mg [1, 2], Al–Cu–Mg [3, 4], and Al–Zn systems [5, 6], which are characterized by a higher degree of mechanical properties when compared to the AlSi10Mg alloy, which has been the most widespread additive technology as of late [7, 8]. The main drawbacks of these materials are high susceptibility to the formation of crystallization cracks due to the broad effective crystallization range and nonhomogeneous structure.

A review of contemporary scientific literature shows a general trend toward designing aluminum alloys containing a large amount of transition metals exceeding manifold their limiting solubility in aluminum. This fact is related to the low solubility of transition-metal additives in aluminum (Mn, Fe, Cr, Ti, Zr, Sc, V), which form intermetallide phases possessing high thermal stability due to their low diffusion coeffi-

cient (10^{-14}–10^{-12} cm^2/s at a temperature of 500°C [9, 10]) when compared with conventional alloying elements, such as Si, Zn, Mg, and Cu.

Such a specific character of transition metals allows one to prepare aluminum alloys with a unique set of characteristics under particular conditions: high weldability, high strength, and thermal stability [10–12]. In particular, the high cooling rates upon crystallization (10^4–10^6 K/s) that occur in additive technologies provide a high degree of mechanical characteristics at room and elevated temperatures due to the formation of the ultradisperse structure and supersaturated solid solution based on aluminum.

Fe, Mn, Cr, Ni, and Co are the most prospective transition-metal additives, which is clear from the examples of recently developed aluminum alloys possessing the following compositions, wt %[1]: Al–(3–12)Fe–(0.1–3)V–(0.1–3)Si–(1–6)Cu [13], Al–(5–6)Cu–(2.5–3.5)Mg–(0.5–1.25)Mn–(0–5)Ti–(0–3)B–(0–0.15)V–(0–0.15)Zr–(0–0.25)Si–(0–0.25)Fe–(0–0,5)Cr–(0–1)Ni [14], Al–(3–4.5)Si–(0.7–1.5)Mg–(0.5–1)Mn–(0–0.5)Fe–(0–0.1)Cu–(0–0.5)Ti–(0–0.2)B–(0–1.5)Ni [15]. Russian researchers have developed alloys based on the Al–12Si–Ni–Fe [16] and Al–(2.5–9.5)Ni–2.5Fe systems [17] for additive technologies which are characterized by high strength and thermal stability at 300–350°C.

The main drawback of alloying with transition metals at large concentrations of aluminum alloys dedicated for additive technologies is the possibility of formation of coarse primary crystals of intermetallide phases due to nonuniform cooling conditions. Therefore, controlling cooling conditions during the "growth" of the products from aluminum alloys doped with transition metals using additive technologies is an important task.

An alloy based on the Al–Fe–Mn system which is promising for the development of high-strength thermally stable aluminum alloys for additive technologies due to Al_3Fe and Al_6Mn intermetallide phases [10] was investigated in this work. The formation of its structure depending on the cooling rate upon crystallization during casting and laser melting was studied and recommendations on the conditions of laser melting of this alloy for its further use in additive technologies were developed.

PROCEDURE OF EXPERIMENTS

An alloy with the composition of Al–2.5Fe–1.5Mn was fused from pure aluminum (A99 brand) and Al–10Fe and Al–10Mn alloying compositions in a Nabertherm S3 electrical furnace. In order to provide a different cooling rate ($v_{cooling}$), the ingots possessed various cross sections upon crystallization. The ingots possessing ∅6 mm were prepared by casting into a thick-wall copper mold ($v_{cooling}$ = 940 K/s), those with ∅14 mm were prepared by casting into a steel mold ($v_{cooling}$ = 26 K/s), and those with ∅100 mm were prepared by casting into graphite mold ($v_{cooling}$ = 0.5 K/s). The cooling rate was controlled using a chromel–alumel thermocouple mounted at the half-height of the mold. The experiment was performed at an identical recording frequency corresponding to 1 kHz at all cooling rates. The temperature of melt corresponded to 700°C before casting.

Laser melting was performed on specimens 2 mm in thickness. Fusion of the surface of the specimens in the form of single tracks was carried out on an MUL-1-M-200 repetitively pulsed instrument equipped with a Nd–YAG-fiber laser with a radiation wavelength of 1064 nm using the following parameters: laser power 34.6 W, scanning rate 1 mm/s, pulse length 12 ms, and eclipse 0.2 mm.

The X-ray phase analysis (XPA) of the cast alloys was performed on a Bruker Advance D8 diffractometer at intrinsic radiation of CuK_α (λ = 0.154051 nm) with the step of 2θ = 0.05°. Microstructural analysis and X-ray microanalysis (XMA) of the alloys in cast state and after laser melting were carried out using a TESCAN VEGA 3LMH scanning electron microscope equipped with an XMAX-80 adapter in the reflected electron mode. The shots were prepared using a Struers-Labopol-5 instrument. The polished surface was additionally exposed to anodic polishing in a 30% alcohol solution of $HClO_4$ (the temperature of electrolyte was less than 5°C) at a voltage of 25 V.

Using differential scanning calorimetry (DSC), the temperature of the solidus of the alloys was measured using a Setaram Labsys calorimeter in an argon atmosphere at a heating rate of 0.667 K/s.

Microhardness after laser melting was measured on polished specimens etched with a Keller solution (5HCl–5HNO_3–3HF) using the Vickers method on a Wolpert microhardness meter with a load of 500 g and an exposure time of 10 s. The mean microhardness values were calculated for each specimen (according to ten indentations). The yield strength was determined by the calculation of the Orovan stress (the stress required to achieve the formation mechanism of dislocation loops around eutectic inclusions), assuming the uniform distribution of eutectic inclusions using the following equation [18]:

$$\tau_p = \frac{0.81Gb}{2\pi\sqrt{1-\nu}(\lambda - m)} \ln\frac{m}{r_0},$$

where G is the shear modulus, MPa; b is the Burgers vector, m; ν is the Poisson coefficient, m/m; m is the mean inclusion diameter, m; λ is the distance between the centers of inclusions, m; $r_0 \approx 1.5b$; and $L = \lambda - m$ is the distance between the surfaces of inclusions.

Using the Thermo-Calc program package, polythermal sections of the Al–Fe–Mn were plotted and

[1] Here and elsewhere, wt % is implied unless otherwise noted.

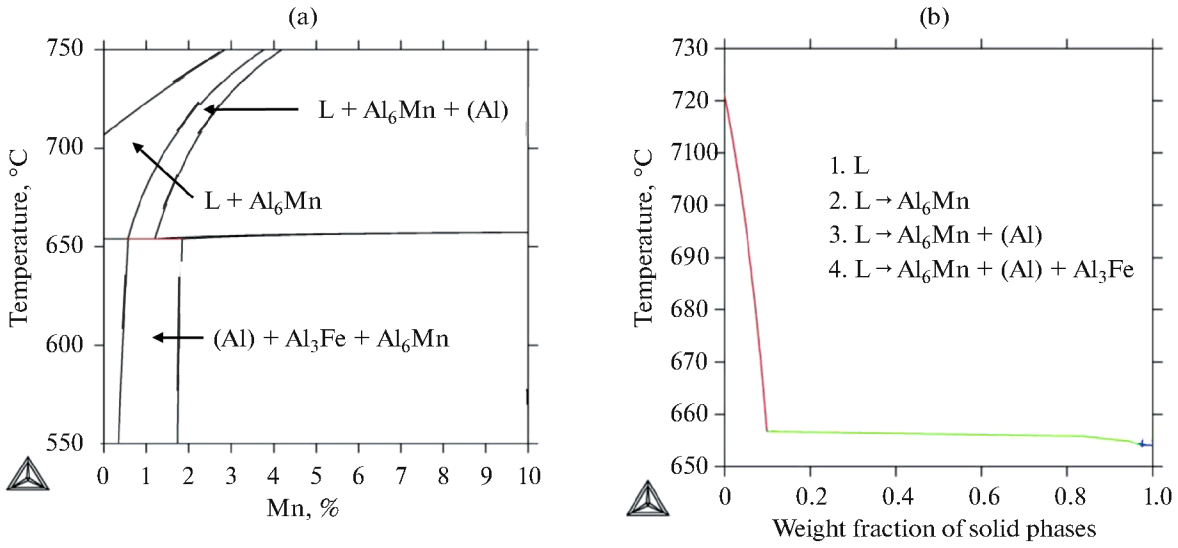

Fig. 1. (a) Polythermal cross section of the Al–2.5Fe–(0–10)Mn systems and (b) calculation of the change in the weight fraction of solid phases in the Al–2.5Fe–1.5Mn alloy.

the change in the weight fraction of solid phases in the Al–2.5Fe–1.5Mn alloy was calculated according to the Scheil curve.

RESULTS AND DISCUSSION

Manganese and iron from the aluminum side form a diagram of the state of the eutectic type. Figure 1a shows the polythermal section of the Al–2.5Fe–(0–10)Mn system. The phases of (Al), Al_3Fe, and Al_6Mn are present in the equilibrium state at the content of 0.3 to 1.8% of manganese and 2.5% iron in the alloy. As can be seen from the results of a calculation of the phase composition of the alloys in the ternary region of the diagram of state, the volume fraction of the Al_6Mn intermetallide phase amounts to 16.3%, with an increase in the manganese content to 1.5% (Table 1). Thus, an increased content of intermetallide phases in the alloys provides higher characteristics after laser treatment.

Table 1. Calculated values of the number of phases, temperatures of formation of 65% of solid phases, nonequilibrium solidus, and ECR (Thermo-Calc)

Alloy	Content, vol %			$t_{65\%}$, °C	t_{ns}, °C	ECR
	Al_3Fe	Al_6Mn	(Al)			
Al–2.5Fe–0.5Mn	2.3	11.1	86.6	656	653	3
Al–2.5Fe–1.5Mn	2.5	16.3	81.2	656	654	2

The values of effective crystallization range (ECR) of the Al–2.5Fe–1.5Mn alloy, calculated using the Thermo-Calc program (Fig. 1b) as the difference between the temperature of formation of the 65% fraction of solid phases and temperature of solidus [19], are also given in Table 1. It can be seen that the alloy possesses narrow ECR, which should provide its high cast characteristics and high weldability, which allows one to reduce the number of defects at laser melting.

Using DSC method, it was determined that the experimental temperature of the solidus of the Al–2.5Fe–1.5Mn alloy corresponds to 655°C, which is much higher than that of conventional AlSi10Mg alloy for additive technologies (t_{ns} = 557°C [20]) and can provide high thermal stability.

Figure 2 shows microstructures of the Al–2.5Fe–1.5Mn alloy obtained at various cooling rates in the crystallization range. The appearance of local peaks in Fig. 2c is related to the relatively small scale (the amount of data within 0.1 s) when compared to the plots in Figs. 2a and 2b.

The phase composition and distribution map of alloying elements of the alloy are given in Figs. 3 and 4. Almost any crystallization of alloys under laboratory and industrial conditions is nonequilibrium, which is determined by the deviation of mean composition and volume fractions of solid phases from theoretical values. The structure of the specimen crystallized at a low cooling rate of 0.5 K/s (Fig. 2a) is similar to the equilibrium state. The main structural components are represented by large primary

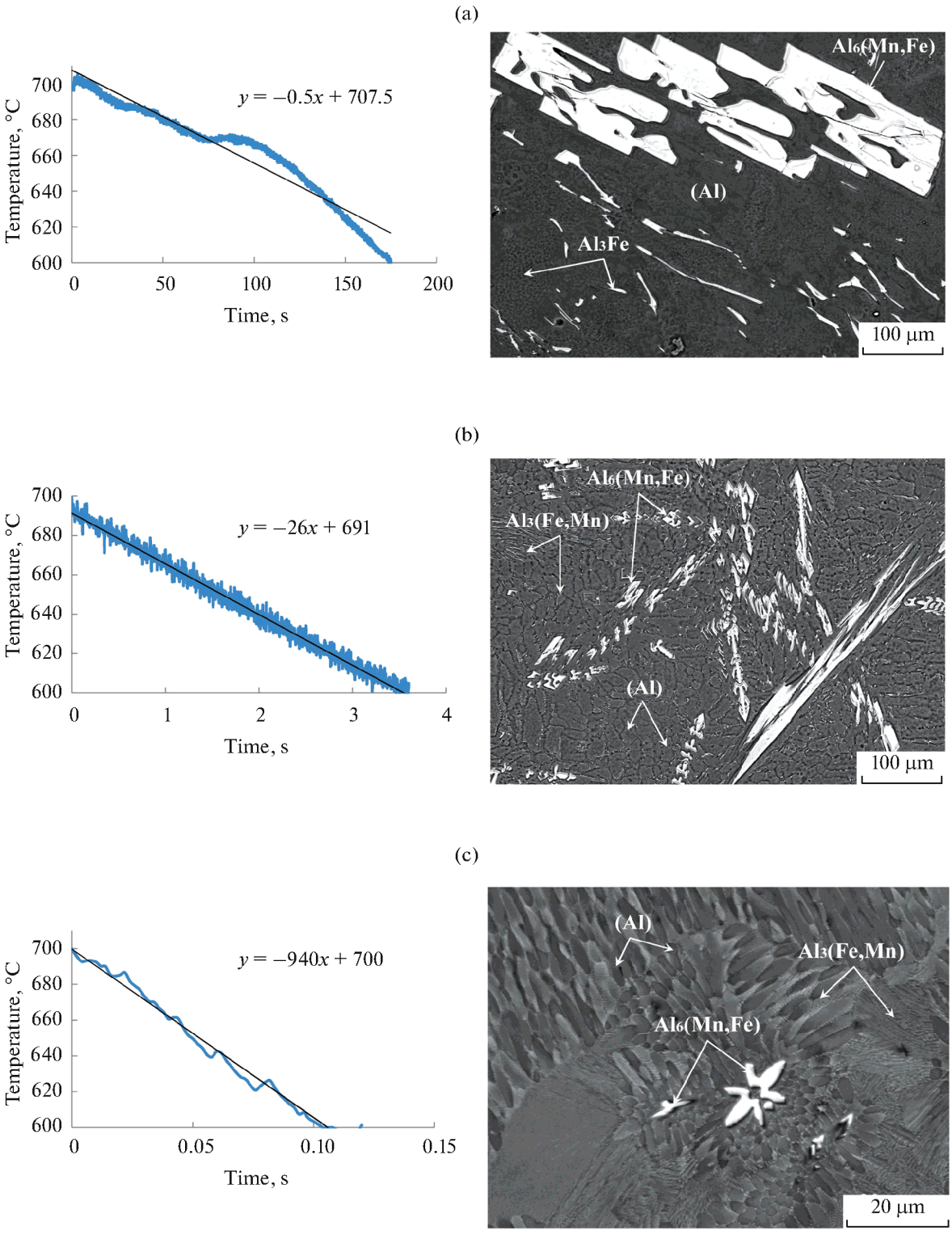

Fig. 2. Typical microstructures of the Al–2.5Fe–1.5Mn alloy obtained at the cooling rates of (a) 0.5, (b) 26, and (c) 940 K/s.

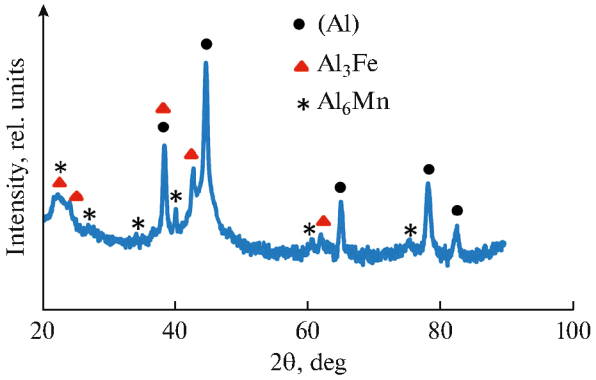

Fig. 3. X-ray diffractogram of the Al–2.5Fe–1.5Mn alloy in the cast state ($v_{cooling}$ = 26 K/s).

crystals of the $Al_6(Mn,Fe)$ phase, which occupy 35% of the volume; a solid solution based on aluminum (Al); and an Al_3Fe phase of eutectic origin, in which the mean plate thickness is 2.7 ± 0.1 μm.

With an increase in the cooling rate to 26 K/s, crystallization occurs under conditions further from equilibrium, which leads to an increase in the nonequilibrium content of the $Al_3(Fe,Mn)$ eutectic phase located along the boundaries of aluminum solid solution up to 15%. The mean plate size of the eutectic phase corresponds to 1.5 ± 0.1 μm, while the interlamellar distance is 2.3 μm. The size of dendritic cell (Al) amounts to 12.6 ± 1.1 μm. The size of primary crystals decreases from 210 to 54 μm (Fig. 2b).

Using the XMA method, it was determined that the Al_6Mn phase contains partially dissolved iron, whereas Al_3Fe contains manganese (Fig. 4).

With an increase in the cooling rate to 940 K/s, the microstructure changes remarkably (Fig. 2c): the mean size of dendritic cells (Al) decreases to 1.8 ± 0.1 μm, the volume fraction of nonequilibrium eutectics increases to 43%, the mean size of eutectic plates decreases to 0.3 ± 0.01 μm, and the interlamellar distance decreases to 0.4 ± 0.02 μm. At this cooling rate, the nearly total suppression of primary crystallization

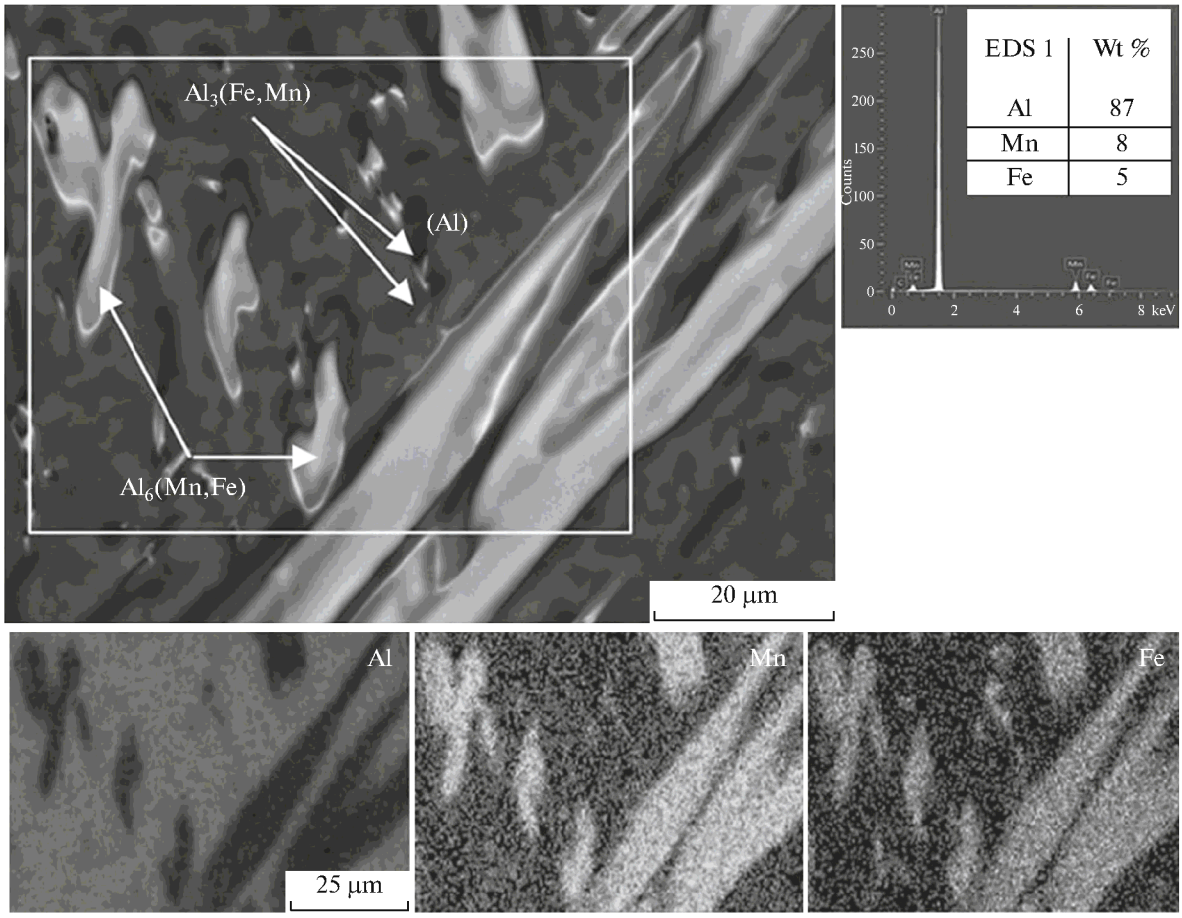

Fig. 4. Microstructure and distribution maps of alloying elements recorded in the intrinsic X-ray radiation of AlK_α, MnK_α, and FeK_α using XMA ($v_{cooling}$ = 26 K/s).

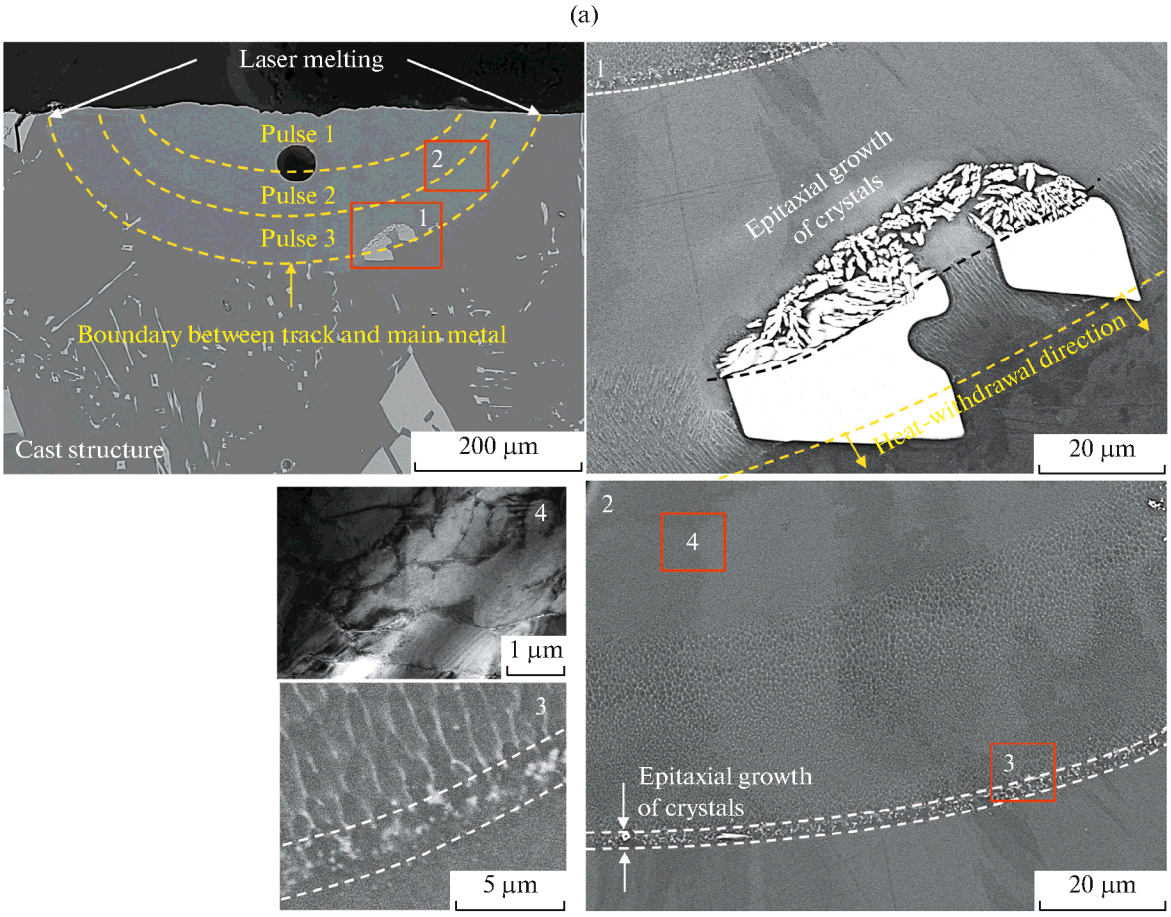

Fig. 5. Microstructure of the profiles of single tracks after laser melting of the Al–2.5Fe–1.5Mn alloy with various types of initial cast structure obtained at $v_{cooling}$ = (a) 0.5, (b) 26, and (c) 940 K/s.

of the $Al_6(Mn,Fe)$ phase occurs and its volume fraction decreases to 3.5%.

Thus, manganese is included in the eutectic phase of $Al_3(Fe,Mn)$ and can dissolve in aluminum solid solution.

It can be seen from the dynamics of the change in the microstructure of the Al–2.5Fe–1.5Mn alloy prepared under various crystallization conditions that primary crystallization is almost completely suppressed with an increase in the cooling rate to 940 K/s, and there is a transition to dendritic crystallization with the formation of a large volume fraction of the eutectic phase.

At the second stage of investigation, the surface of the cast specimens crystallized at various cooling rates was exposed to laser melting. Microstructures of single tracks after such treatment are given in Fig. 5.

The microstructure of the track melted on the surface of the specimens with the initial structure obtained at $v_{cooling}$ = 0.5 K/s was characterized by a disperse structure with a predominantly dendritic shape of the crystals of aluminum solid solution surrounded by the particles of the iron–manganese phase, which was formed during eutectic crystallization (Fig. 5a). A dendritic structure was formed in the track at the boundary between track and main (cast) metal, where aluminum solid solution was used as a substrate, except for the domain including primary crystals of the $Al_6(Mn,Fe)$ phase in the laser melting zone.

Laser exposure on the material resulting in the melting of a small region takes few tenths of a second. The partial fusion of the $Al_6(Mn,Fe)$ phase occurs within a short time interval (the suggested boundary of fusion is indicated by a black dashed line) with subsequent fast crystallization in the form of disperse particles. The form of arrangement of crystallized particles indicates their susceptibility to epitaxial growth in the presence of a substrate in the form of the unfused phase (Fig. 5a, region *1*). The same region of epitaxial growth with a width of 1.9 μm is formed at the boundary of the 2nd and 3rd pulses (Fig. 5a, region *3*). Its appearance can be caused by the fact that the iron–manganese phase crystallizes from the melt on eutec-

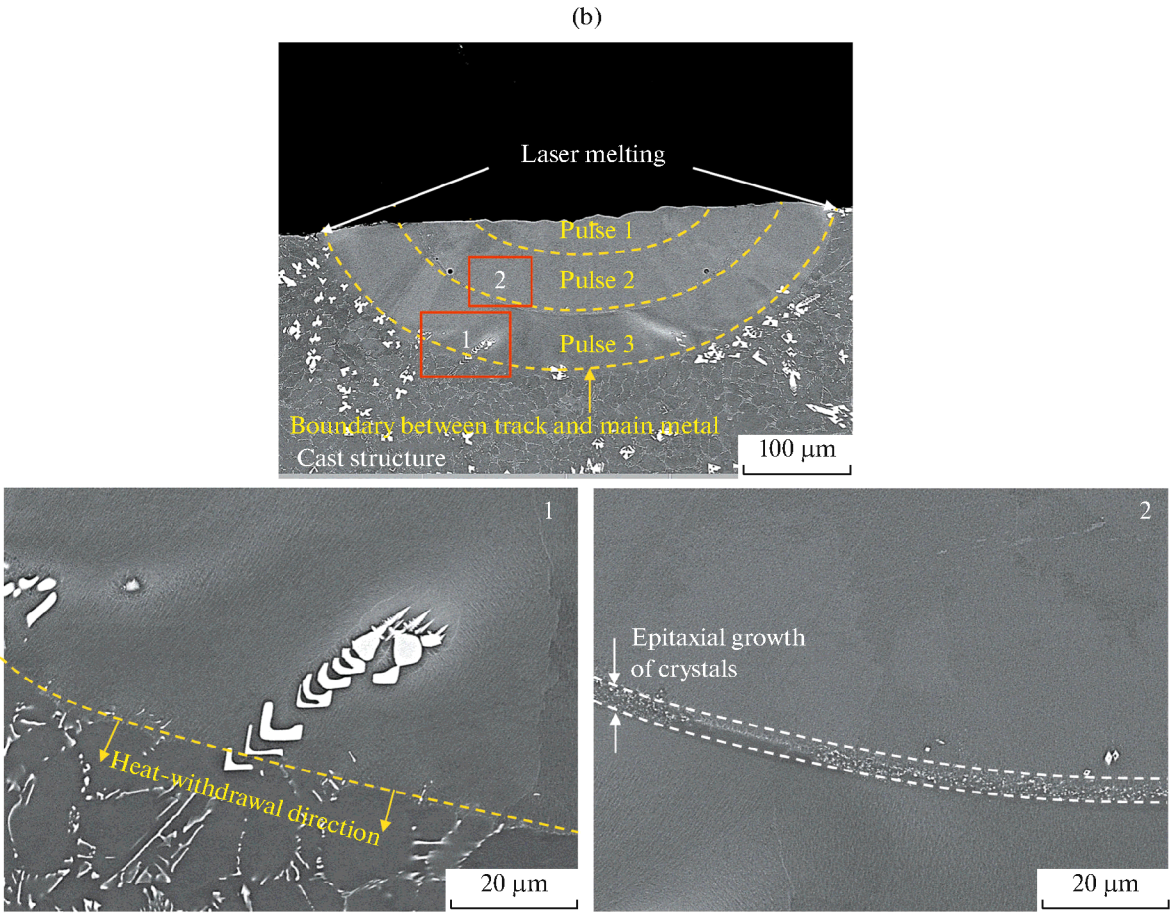

Fig. 5. (Contd.)

tic particles of the same phase in the lower unfused layer. As the distance from the fusion boundary increases, the structure is replaced by dendritic (Fig. 5a, region *4*). The mean dendritic size of the matrix corresponds to 0.68 ± 0.08 μm at the boundary with main metal, while this size is 0.56 ± 0.05 μm in the central region.

Derived from the dependence of the dendritic parameter on the cooling rate upon crystallization, the cooling rates during laser melting were evaluated. It can be stated according to the results of calculations that the values of $v_{cooling}$ vary from 1.1×10^4 at the boundary with main metal to 2.5×10^4 K/s in the central region, which corresponds to the cooling rates upon crystallization realized in additive technologies [21–25].

The microstructure of the track fused on the surface of the specimen with the initial structure obtained at $v_{cooling} = 26$ K/s is given in Fig. 5b. It is characterized by a disperse structure with a predominantly dendritic shape of the crystals of aluminum solid solution surrounded by particles of the iron–manganese phase, which was formed according to eutectic reaction.

Primary crystals of the $Al_6(Mn,Fe)$ phase and eutectic particles of the $Al_3(Fe,Mn)$ phase were exposed to remelting at the boundary between the track and the main metal (Fig. 5b, region *1*). The particles of the mentioned phases are also detected in the track structure in these regions; however, they are smaller in size, which indicates the epitaxial character of crystallization. As in the previous track (Fig. 5a), a thin interlayer from primary crystals of the iron–manganese phase, formed as a result of epitaxial growth, is formed at the boundary of two pulses. Its mean width corresponds to 2 μm, whereas the size of primary crystals is less than 1 μm (Fig. 5b, region *2*).

Figure 5c shows the microstructure of the track fused on the surface of the specimen with the initial structure obtained at $v_{cooling} = 940$ K/s. Here, crystallization of the region remelted with laser started on the solid substrate consisting of crystals of dendritic type. The eutectic phase of $Al_3(Fe,Mn)$ along the boundaries of dendritic cells, whose melting point is lower than that of aluminum solid solution, was fused. Primary crystallization of this phase occurs upon hardening, which can be seen from the differences in microstruc-

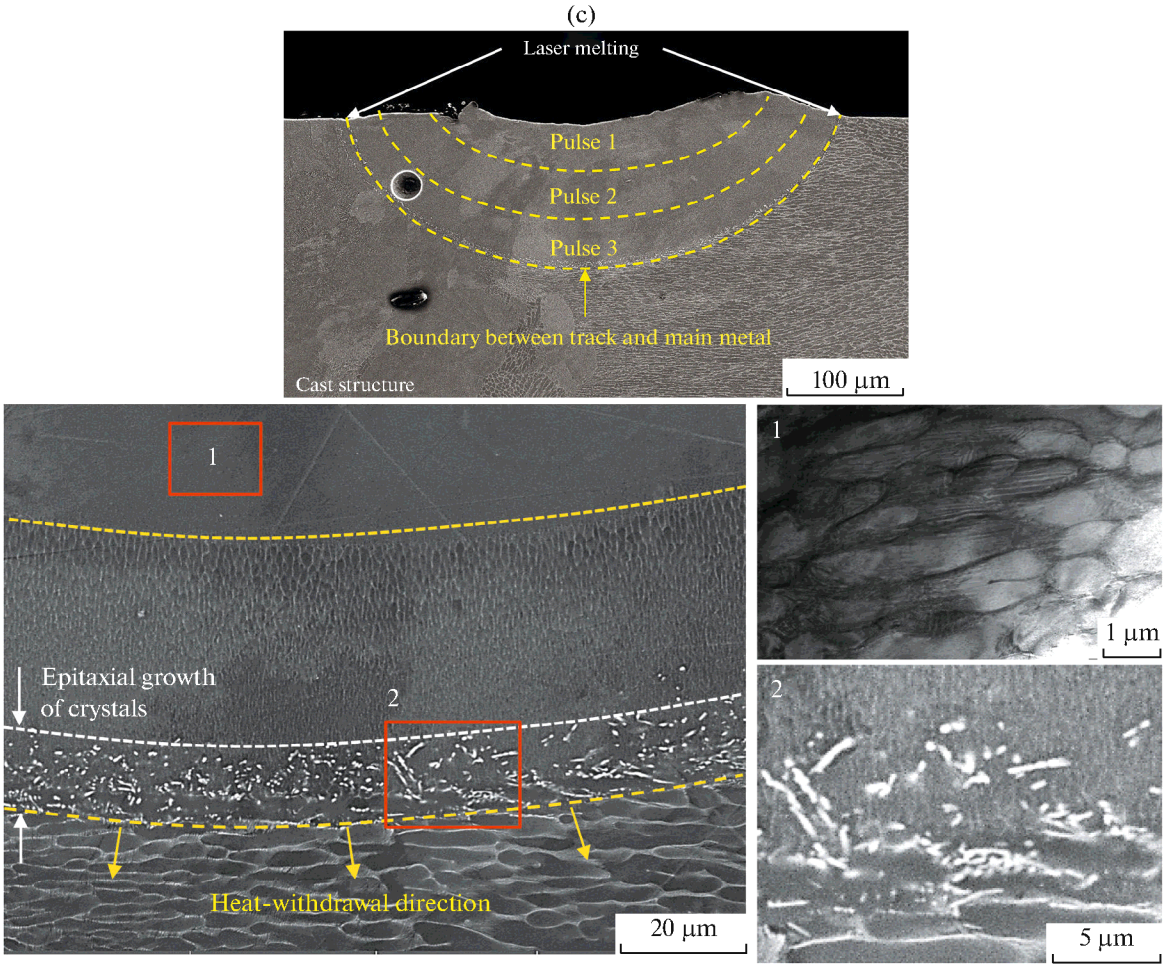

Fig. 5. (Contd.)

ture (Fig. 5c, region *2*). The size of primary crystals is less than 4 μm, while the width of the region of their epitaxial growth is larger than that between pulses and corresponds to 9.5 μm. This can be caused by the fact that the initial size of eutectic plates exposed to remelting is larger in the lower layer than that in the track structure. The microstructure also possesses a dendritic structure with a mean cell size of 0.65 ± 0.06 μm far from the boundary with the main metal.

As follows from an analysis of track microstructure obtained upon laser melting (with the assumption of a similar cooling rate), such a structure would be formed in the alloy when using it as a powder in additive technologies, in particular, upon selective laser melting. The formation of narrow domains consisting of primary crystals of iron–manganese phase as a result of their epitaxial growth should be anticipated at the boundary of tracks and layers in this product. On the whole, the structure of all tracks prepared during laser melting is characterized by the absence of crystallization cracks, which is rationalized by the narrow ECR of the Al–2.5Fe–1.5Mn alloy.

The hardness of the alloy in the case state varies from 37 to 67 HV with an increase in the cooling rate upon crystallization, which can be caused by the high dispersion of the $Al_3(Fe,Mn)$ phase and the realization of the mechanism of solid-solution hardening due to the increase in the manganese content in (Al). The formation of the ultradisperse microstructure as a result of laser melting results in a significant increase in the hardness of alloy to 93 HV (Fig. 6).

Annealing at temperatures of 100, 200, and 300°C for 1 h resulted in a marginal decrease in hardness to 91 ± 2, 86 ± 1, and 85 ± 1 HV, respectively. An increase in the temperature of annealing to 400°C gave rise to a larger drop of hardness to 64 HV. The high thermal stability of the Al–2.5Fe–1.5Mn alloy after laser melting can be caused by the stability of the intermetallide Fe–Mn phase of eutectic origin due to the low diffusion coefficient of manganese and iron in the aluminum solid solution [10].

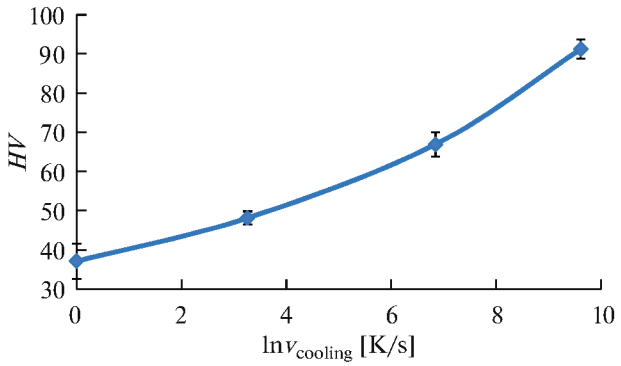

Fig. 6. Dependence of hardness on the cooling rate of the Al–2.5Fe–1.5Mn alloy.

The yield strength of the Al–2.5Fe–1.5Mn alloy with the structure obtained upon laser melting was calculated. Uniform particle distribution of the second phase of eutectic origin was considered, with the mean size of 0.28 μm, whereas the mean distance between them is 0.56 μm, which corresponded to the mean size of the dendritic cell. The calculated yield strength of the alloy corresponded to 227 MPa.

Thus, it can be stated that combination of high characteristics of the Al–2.5Fe–1.5Mn alloy, such as dispersion of the structure formed at laser melting, hardness at room and elevated temperatures, and the calculated yield strength, renders it promising for additive technologies.

CONCLUSIONS

(1) Features of formation of microstructure in the alloy based on aluminum alloyed with Fe and Mn have been studied depending on the cooling rate upon casting and during laser melting.

(2) It has been shown that the microstructure of the Al–2.5Fe–1.5Mn alloy in the case state prepared at a cooling rate of 0.5 K/s consists of large primary crystals of the Al_6(Mn,Fe) phase, a solid solution based on aluminum (Al), and the Al_3Fe phase of eutectic origin. An increase in the cooling rate to 26 K/s results in the formation of (Al) in the form of dendrites with a mean cell size of 12.6 μm and an increase in the nonequilibrium fraction of the Al_3(Fe,Mn) eutectic phase along the boundaries of the aluminum solid solution up to 15%. With an increase in the cooling rate to 940 K/s, the primary crystallization of the Al_6(Mn,Fe) phase is almost completely suppressed, the mean size of dendritic cells of (Al) decreases to 1.8 μm, and the volume fraction of nonequilibrium eutectics increases to 43%.

(3) An analysis of the microstructure of the Al–2.5Fe–1.5Mn alloy after laser melting has shown that the crystals of the aluminum matrix of dendritic type with a mean cell size of 0.56 μm surrounded by the iron–manganese phase of eutectic origin with the mean plate size of 0.28 μm are formed in the bulk. Primary crystallization of the Al_6(Mn,Fe) phase is completely suppressed. It has been determined that the formation of such a structure occurs at cooling rates of $(1.1–2.5) \times 10^4$ K/s.

(4) The domains at the boundary between the track and main metal, as well as on the boundary of repeated melting consisting of primary crystals of the Al_6(Mn,Fe) phase, which are formed through the epitaxial growth mechanism, have been revealed. The smaller the eutectic plates and dendritic cell in the epitaxial layer are, the more dispersed the primary crystals in the remelting zone are.

(5) It has been shown that the Al–2.5Fe–1.5Mn alloy possesses high hardness corresponding to 93 HV after laser melting. Its microstructure is characterized by high thermal stability, which is confirmed by the retention of high hardness (85 HV) upon heating to 300°C. The calculated yield strength of this alloy is 227 MPa.

FUNDING

This work was supported by the Russian Foundation for Basic Research (project no. 19-38-60037).

CONFLICT OF INTEREST

The authors declare that they have no conflict of interest.

REFERENCES

1. Li, R., Wang, M., Yuan, T., Song, B., Chen, C., Zhou, K., and Cao, P., Selective laser melting of a novel Sc and Zr modified Al–6.2Mg alloy: Processing, microstructure, and properties, *Powder Technol.*, 2017, vol. 319, pp. 117–128.
2. Spierings, A.B., Dawson, K., Heeling, T., Uggowitzer, P.J., Schäublin, R., Palm, F., and Wegener, K., Microstructural features of Sc- and Zr-modified Al–Mg alloys processed by selective laser melting, *Mater. Des.*, 2017, vol. 115, pp. 52–63.
3. Zhang, H., Zhu, H., Nie, X., Yin, J., Hu, Z., and Zeng, X., Effect of zirconium addition on crack, microstructure and mechanical behavior of selective laser melted Al–Cu–Mg alloy, *Scr. Mater.*, 2017, vol. 134, pp. 6–10.
4. Lopez-Botello, O., Martinez-Hernande, U., Ramírez, J., Pinna, C., and Mumtaz, K., Two-dimensional simulation of grain structure growth within selective laser melted AA-2024, *Mater. Des.*, 2017, vol. 113, pp. 369–376.
5. Jiang, B., Zhenglong, L., Xi, C., Peng, L., Nannan, L., and Yanbin, C., Microstructure and mechanical properties of TiB_2-reinforced 7075 aluminum matrix composites fabricated by laser melting deposition, *Ceram. Int.*, 2019, vol. 45, pp. 5680–5692.
6. Qi, T., Zhu, H., Zhang, H., Yin, J., Ke, L., and Zeng, X., Selective laser melting of Al7050 powder: Melting mode transition and comparison of the characteristics

between the keyhole and conduction mode, *Mater. Des.,* 2017, vol. 135, pp. 257–266.

7. Zhang, J., Song, B., Wei, Q., Bourell, D., and Shi, Y., A review of selective laser melting of aluminum alloys: Processing, microstructure, property and developing trends, *J. Mater. Sci. Technol.,* 2019, vol. 35, pp. 270–284.
8. Biffi, C.A., Fiocchi, J., Bassani, P., Paolino, D.S., Tridello, A., Chiandussi, G., Rossetto, M., and Tuissi, A., Microstructure and preliminary fatigue analysis on AlSi10Mg samples manufactured by SLM, *Procedia Struct. Integr.,* 2017, vol. 27, pp. 50–57.
9. Hirano, K., Agarwala, R., and Cohen, M., Diffusion of chromium in aluminium, *Acta Metall.,* 1962, vol. 10, pp. 857–863.
10. Dobatkin, V.I. and Elagin, V.I., *Granuliruemye alyuminievye splavy* (Pelletized Aluminum Alloys), Moscow: Metallurgiya, 1981.
11. Belov, N.A., Eskin, D.G., and Avxentieva, N.N., Constituent phase diagrams of the Al–Cu–Fe–Mg–Ni–Si system and their application to the analysis of aluminium piston alloys, *Acta Mater.,* 2005, vol. 53, no. 17, pp. 4709–4722.
12. Eskin, D.G., Suyitno, and Katgerman, L., Mechanical properties in the semi-solid state and hot tearing of aluminium alloys, *Prog. Mater. Sci.,* 2004, vol. 49, no. 5, pp. 629–711.
13. Karbin, L.M., Yanar, C., Heard, D.W., and Wang, W., US Patent 2016/0138400 A1, 2016.
14. Wentland, W.L., Karlen, E., Mironets, S., Ocken, T.J., and Bianco, R., US Patent 2017/0016096 A1, 2017.
15. Wentland, W.L., Karlen, E., Mironets, S., Ocken, T.J., and Bianco, R., US Patent 2017/0016094A1, 2017.
16. Manca, D.R., Churyumov, A.Yu., Pozdniakov, A.V., Ryabov, D.K., Korolev, V.A., and Daubarayte, D.K., Novel heat-resistant Al–Si–Ni–Fe alloy manufactured by selective laser melting, *Mater. Lett.,* 2019, vol. 236, pp. 676–679.
17. Loginova, I.S., Churyumov, A.Yu., Daubarayte, D.K., Korolev, V.A., and Solonin, A.N., The effect of transition metal additives Fe, Cr, Mn, and Ni on the structure and properties of aluminum alloys under laser irradiation in additive technologies, *Tekhnol. Legk. Splavov,* 2019, no. 4, pp. 5–16.
18. Churyumov, A.Yu., Calculation of the yield strength and strain hardening of aluminum alloys by structural parameters, *Extended Abstract of Cand. Sci. (Eng.) Dissertation,* Moscow: National Univ. of Science and Technology MISiS, 2008.
19. Pozdnyakov, A.V., Zolotorevskii, V.S., and Khomutov, M.G., *Goryachelomkost' liteinykh alyuminievykh splavov* (Hot Brittleness of Aluminum Casting Alloys), Moscow: National Univ. of Science and Technology MISiS, 2014.
20. Vončina, M., Mrvar, P., and Medved, J., Thermodynamic analysis of AlSi10Mg alloy, *RMZ—Mater. Geoenviron.,* 2006, vol. 52, no. 3, pp. 621–633.
21. Pozdniakov, A.V., Churyumov, A.Y., Loginova, I.S., Daubarayte, D.K., Ryabov, D.K., and Korolev, V.A., Microstructure and properties of novel AlSi11CuMn alloy manufactured by selective laser melting, *Mater. Lett.,* 2018, vol. 225, pp. 33–36.
22. Churyumov, A.Yu., Pozdniakov, A.V., Prosviryakov, A.S., Loginova, I.S., Daubarayte, D.K., Ryabov, D.K., Korolev, V.A., Solonin, A.N., Pavlov, M.D., and Valchuk, S.V., Microstructure and mechanical properties of a novel selective laser melted Al–Mg alloy with low Sc content, *Mater. Res. Express,* 2019, vol. 6, p. 126595.
23. Kaplanskii, Yu.Yu., Sentyurina, Zh.A., Loginov, P.A., Levashov, E.A., Korotitskiy, A.V., Travyanov, A.Yu., and Petrovskii, P.V., Microstructure and mechanical properties of the (Fe,Ni)Al-based alloy produced by SLM and HIP of spherical composite powder, *Mater. Sci. Eng., A,* 2019, vol. 743, pp. 567–580.
24. Manca, D.R., Churyumov, A.Y., Pozdniakov, A.V., Prosviryakov, A.S., Ryabov, D.K., Krokhin, A.Y., Korolev, V.A., and Daubarayte, D.K., Microstructure and properties of novel heat resistant Al–Ce–Cu alloy for additive manufacturing, *Met. Mater. Int.,* 2019, vol. 25, no. 3, pp. 633–640.
25. Kaplanskii, Yu.Yu., Zaitsev, A.A., Sentyurina, Zh.A., Levashov, E.A., Pogozhev, Yu.S., Loginov, P.A., and Logachev, I.A., The structure and properties of pre-alloyed NiAl–Cr(Co,Hf) spherical powders produced by plasma rotating electrode processing for additive manufacturing, *J. Mater. Res. Technol.,* 2018, vol. 7, no. 4, pp. 461–468.

Translated by A. Muravev